applied sciences

MDPI

Article

A Systematical Comparison of Catalytic Behavior of NM/γ-Al_2O_3 (NM = Ru, Rh, Pt, Pd, Au, Ir) on 1,2-Dichloroethane Oxidation: Distributions of By-Products and Reaction Mechanism

Lu Li [1], Jingjie Zhang [2], Han Xu [2], Mingjiao Tian [3,*] and Chi He [2,*]

[1] State Key Laboratory of Electrical Insulation and Power Equipment, Center of Nanomaterials for Renewable Energy, School of Electrical Engineering, Xi'an Jiaotong University, Xi'an 710049, China
[2] State Key Laboratory of Multiphase Flow in Power Engineering, School of Energy and Power Engineering, Xi'an Jiaotong University, Xi'an 710049, China
[3] School of Human Settlements and Civil Engineering, Xi'an Jiaotong University, Xi'an 710049, China
* Correspondence: Mingjiao.Tian@xjtu.edu.cn (M.T.); chi_he@xjtu.edu.cn (C.H.)

Featured Application: This work supplies a systematical comparison study on various typical noble metal catalysts with an exploration of the potential for CVOC destruction, which would supply an overall view of universal applicability for the practical operation of noble metals.

Abstract: Understanding the reaction path and mechanism of chlorinated volatile organic compound (CVOC) destruction is important for designing efficient catalysts, especially for the application of noble metal-based materials. Herein, several typical noble metals, Ru, Rh, Pt, Pd, Au, and Ir, supported on γ-Al_2O_3 catalysts were synthesized by the hydrazine hydrate reduction method for 1,2-dichloroethane (1,2-DCE) elimination. Various character measurements were conducted, and the results suggest that the high-valence state of noble metals is beneficial for the 1,2-DCE reaction as it enables the enhancement of the mobility of the surficial active oxygen species of catalysts. Among the noble metals, Ru/γ-Al_2O_3 expresses superior catalytic reactivity, with a 90% pollutant conversion rate at 337 °C, and competitive CO_2 selectivity, 99.15% at the temperature of total oxidation. The distribution of by-products and the degradation routes were analyzed online by GC-ECD and *in situ* diffuse reflectance infrared spectroscopy, which may provide helpful insight for the future application of noble metal-based catalysts for CVOC elimination in industrial fields.

Keywords: 1,2-DCE; noble metal; catalytic oxidation; γ-Al_2O_3; by-products

Citation: Li, L.; Zhang, J.; Xu, H.; Tian, M.; He, C. A Systematical Comparison of Catalytic Behavior of NM/γ-Al_2O_3 (NM = Ru, Rh, Pt, Pd, Au, Ir) on 1,2-Dichloroethane Oxidation: Distributions of By-Products and Reaction Mechanism. *Appl. Sci.* **2023**, *13*, 36. https://doi.org/10.3390/app13010036

Academic Editor: In Sun Cho

Received: 1 November 2022
Revised: 6 December 2022
Accepted: 8 December 2022
Published: 20 December 2022

1. Introduction

As one of the most toxic and complicated kinds of volatile organic compounds (VOCs), chlorinated volatile organic compounds (CVOCs) are usually difficult to eliminate [1,2] due to their high volatility, strong recalcitrance, and their side effects for the operation system [3–5]. CVOCs includes chlorinated alkanes [6,7], chlorinated olefins [8], chlorinated aromatic hydrocarbons [9], etc., which are regarded as vital compounds of common contaminants, which have been widely investigated for years [10,11]. Adsorption [12–14], absorption, condensation and thermal incineration [15], biodegradation [16], photocatalytic degradation [17], plasma technology, and catalytic combustion [4] are applied for elimination of these pollutants. Of which, catalytic oxidation is widely considered as one of the most promising method due to ultra-purification efficiency, few secondary pollution, and lower reaction temperature; therefore it is thought to be one of the most impressive methods for CVOCs elimination.

Currently, the catalysts for CVOC catalytic oxidation can be mainly applied to supported noble metals, molecular sieves, transition metal oxides, perovskite catalysts, etc.

Among these different materials, noble metal-based catalysts have, in recent years, received the attention of many researchers due to their superior low-temperature activity, high CO_2 selectivity, and competitive stability. More importantly, noble metal-based catalysts have been successfully applied practically in various heterogeneous catalytic areas. Few other kinds of materials can be substituted for noble metals in practical operation nowadays [2]. Supported noble metal catalysts are generally catalysts with ruthenium (Ru) [18], platinum (Pt) [19], palladium (Pd) [20], or rhodium (Rh) [21] as active components, and inactive oxides (such as Al_2O_3 [22,23], SiO_2, ZrO_2 [24], TiO_2 [25,26], etc.), molecular sieves [27], perovskite composite oxide $LaBO_3$ [28,29], and pillared clay as carriers. Maupin et al. [23] proposed a bifunctional reaction mechanism of dichloromethane catalyzed by Pt/Al_2O_3, that is, CH_2Cl_2 disproportionated on Al_2O_3 to form CH_3Cl and CO, and then further oxidized on the active site of the Pt metal species. Kaluza et al. [30] believe that the catalytic activity of the catalyst increases with the noble metal loading amount, and the results showed that a Pt/CeO_2-ZrO_2 catalyst with 1% Pt loading is the best. López Fonseca et al. [31] synthesized an H-Beta-supported Pd material for TCE elimination, and the results showed that the 50% conversion of the TCE reaction temperature shifted forward by 150 °C for the molecular sieve supported by precious metal, and PdO was the main active phase, and its activity and stability were better than that of precious metal Pd. At the same time, PdO/H-Beta improves the selectivity of CO_2, but also increases the production of chlorine. Giraudon et al. [32] studied the catalytic decomposition of chlorobenzene over Pd/ZrO_2 and Pd/TiO_2 materials. It was found that, because TiO_2 has higher reducibility than ZrO_2, the Pd/TiO_2 catalyst has better activity, and both catalysts produce a large amount of polychlorinated benzene. In the same year, they found that [33] there was a synergistic effect between the metal Pd and perovskite, which made the catalytic efficiency of $Pd/LaBO_3$ better than that of pure perovskite. Dai et al. [34] prepared the supported Ru/CeO_2 catalyst and found that the dichlorination effect from catalyst surface was promoted due to superior deacon reaction activity of RuO_2, which is beneficial for active sites protection and catalyst stability. Based on the results, the author prepared a series of Ru/Ti-CeO_2 [35] catalysts by doping Ti, and found that the superior combination of 5% Ti doping showed the best reaction performance. Miranda et al. [36] compared the catalytic behavior over trichloroethene of Al_2O_3 supported Pd, Pt, Ru, and Rh materials, the results indicate that the byproduct distribution of Ru-based material was vitally different from other ones. Liu et al. [37] evaluated the detailed polychlorinated byproduct distributions of some noble metals (Pd, Pt, Ru, Rh) loaded on TiO_2 catalysts by an impregnation method for the catalytic destruction of chlorobenzene. As a widely used support material, γ-Al_2O_3 is low-cost and environmentally friendly, which is beneficial for universal application and commercial operation. In fact, many reports have recently pointed out that the catalytic performance of noble metal-based catalysts in the combustion of CVOCs can be improved by introducing different supports, as summarized in Table S1 of Supplementary Information. As a result, noble metals supported on γ-Al_2O_3 are more practical than other types of catalysts, and warrant a systematical discussion of various noble metal-based catalysts. For universal application, the synthesis routine should be simple, economic, and environmentally friendly. On the other hand, at present, only the reaction mechanism of specific pollutants on specific catalysts has been explored, but a universal reaction mechanism on various noble metal catalysts should be investigated to find out whether there is a common route for CVOC oxidation on noble metal materials.

Hence, in this work, we proposed several exemplary noble metals (Ru, Rh, Pt, Pd, Ir, and Au)-based catalysts supported on a common γ-Al_2O_3 material and then systematically investigated their performance on 1,2-dichloroethane (1,2-DCE) oxidation. After characteristic analysis and activity experiments via various measurements, the by-product distribution and detailed oxidation routes were presented to further evaluate the universal reaction mechanism for the purpose of designing superior catalysts.

2. Materials and Methods

2.1. Synthesis of NM (Ru, Rh, Pt, Pd, Au, Ir)/γ-Al_2O_3

The hydrazine hydrate reduction method was used to synthesize the noble metal-based catalysts. Respectively, $RuCl_3$, $(NH_4)_3RhCl_6$, $H_2PtCl_6{\cdot}6H_2O$, $PdCl_2$, $AuCl_3$, and $H_2IrCl_6{\cdot}xH_2O$ were used for each noble metal precursor. During preparation, the loading amount of noble metal was set to 1.0 wt.%. In detail, 1 g of γ-Al_2O_3 (a commercial sample that was purchased from Sigma-Aldrich Co., St. Louis, MO, USA) was dispersed in 60 mL deionized water, 60 mL absolute ethanol, and 20 mL precious metal precursor solution by ultrasonic for about 30 min, followed by stirring for another 20 min to mix evenly. Afterward, the mixture was transferred into a three-neck flask. The mixture was then saturated by N_2, 0.01 g $NaBH_4$ in 20 mL 0.5 M NaOH solution as an alkaline regulator and 6 mL hydrazine hydrate solution, while a reducing agent was added dropwise into the mixture under stirring by a peristaltic pump. After 4 h, the suspension blend was filtered, washed with deionized water and ethanol several times, and then the resultant solid was dried at 100 °C for 10 h. The final products were calcined at 450 °C for 4 h at a heating rate of 2 °C/min. The catalysts were denoted as Ru/γ-Al_2O_3, Rh/γ-Al_2O_3, Pt/γ-Al_2O_3, Pd/γ-Al_2O_3, Ir/γ-Al_2O_3, and Au/γ-Al_2O_3.

2.2. Reactivity Evaluation

The catalytic activity was assessed in a fixed-bed reactor (I.D. = 10 mm). With each batch tested, 0.3 g of the prepared catalysts (40–60 mesh) was put at the center of a quartz reactor. Moreover, 1000 ppm of 1,2-DCE diluted in air with a flow rate of 300 mL/min was used as the inlet reaction stream, recalculated as a gas hourly space velocity (GHSV) of approximately 36,000 $mL{\cdot}g^{-1}{\cdot}h^{-1}$. The concentration of 1,2-DCE and the organic by-products was measured using an online gas chromatograph (GC9890, China) equipped with an electron capture detector (ECD). The content of CO and CO_2 from the outlet gas flow was analyzed by an online gas chromatograph (GC9890A, China) equipped with a flame ionization detector (FID) and nickel converting equipment, similar to that reported by our group previously [38–40]. The 1,2-DCE conversion efficiency and the yield of CO and CO_2 were determined using the following equations:

$$X_{1,2-\mathrm{DCE}} = \frac{C_{\mathrm{in}} - C_{\mathrm{out}}}{C_{\mathrm{in}}} \times 100\% \quad (1)$$

$$Y_{\mathrm{CO}} = \frac{C_{\mathrm{CO}}}{2C_{\mathrm{in}} \times X_{1,2-\mathrm{DCE}}} \times 100\% \quad (2)$$

$$Y_{\mathrm{CO_2}} = \frac{C_{\mathrm{CO_2}}}{2C_{\mathrm{in}} \times X_{1,2-\mathrm{DCE}}} \times 100\% \quad (3)$$

where C_{in}, C_{out} are the 1,2-DCE concentration before and after the reaction, respectively, and C_{CO} and $C_{\mathrm{CO_2}}$ are the outlet consistent of CO and CO_2, respectively.

The normalized reaction rate ($r_{1,2\text{-DCE}}$, $mmol{\cdot}g^{-1}{\cdot}s^{-1}$) was derived using Equation (4):

$$r_{1,2-\mathrm{DCE}} = \frac{X_{1,2-\mathrm{DCE}} \times V_{1,2-\mathrm{DCE}}}{W_{\mathrm{cat}}(wt\%\mathrm{NM})} \quad (4)$$

where W_{cat} is the amount of catalyst (g), wt% NM is the weight ratio of noble metal in the catalyst (%), while $V_{1,2\text{-DCE}}$ is the 1,2-DCE gas flow rate ($mol\ s^{-1}$).

When the reaction efficiency of 1,2-DCE is below 15%, the reaction rate would be described as an alternative formula, as follows:

$$r_{1,2-\mathrm{DCE}} = A \exp\left(\frac{E_a}{RT}\right) P_{1,2-\mathrm{DCE}}^{\alpha} P_{\mathrm{O_2}}^{\beta} \quad (5)$$

where E_a represents the apparent activation energy (J mol^{-1}), R delegates the ideal gas constant (J mol^{-1} K^{-1}), T is the test temperature (K), P^{α} represents the fractional pressure of 1,2-DCE (Pa), and P^{β} is fractional pressure of O_2 (Pa).

Activation energies were calculated at low temperatures for 1,2-DCE conversion efficiencies lower than 15%, which is determined by the Arrhenius relationship via Equation (5) simplified into Equation (6):

$$\ln r = \frac{-E_a}{RT} + C \quad (6)$$

The turnover frequency was calculated using the following equation:

$$TOF = \frac{C_{\mathrm{DCE}} \times X_i \times \nu}{\frac{m_{NM}}{M_{NM}} \times D_i} \quad (7)$$

where X_i represents the 1,2-DCE conversion efficiencies of different catalysts at certain temperatures; C_{DCE} is the feed concentration of 1,2-DCE (mol L^{-1}), ν is the volumetric flow rate (L s^{-1}), M_{NM} is the molecular weight of NM (g mol-1), m_{NM} is the NM loading on the catalyst (g), and D_i is the NM dispersion (%) on the catalyst surface obtained from the CO-chemisorption results.

2.3. Catalyst Characterizations

Various measurements were conducted to characterize the physiochemical properties of the prepared samples, including inductively coupled plasma-optical emission spectroscopy (ICP-OES), X-ray diffraction (XRD), N_2 adsorption-desorption measurements, field-emission scanning electron microscopy (FE-SEM), high-resolution transmission electron microscopy (HR-TEM) images, H_2 temperature-programmed reduction (H_2-TPR), O_2 temperature-programmed desorption (O_2-TPD), NH_3 temperature-programmed desorption (NH_3-TPD) experiments, pulsed CO chemisorption measurements, X-ray photoelectron spectroscopy (XPS) analysis, etc. The detailed descriptions are listed in Supporting Information.

2.4. In Situ DRIFTS Experiments

To deeply explore the kinetics of 1,2-DCE oxidation over the noble metal catalysts, in situ diffuse reflectance infrared spectroscopy (in situ DRIFTS) experiments were implemented and the details are illustrated in Supporting Information.

3. Results and Discussion

3.1. Catalyst Activity Performance

The reaction activity and apparent activation energies of 1,2-DCE over the (Ru, Rh, Pt, Pd, Ir, and Au)/γ-Al_2O_3 materials were tested and calculated, and are exhibited in Figure 1a. As shown, the catalytic performance of the prepared catalysts can destruct 1,2-DCE below 400 °C. By comparing the prepared materials at T_{90} (the reaction temperature of 90% of 1,2-DCE conversion), the conversion efficiencies of all prepared catalysts can be ordered as follows: of Ru/γ-Al_2O_3 (337 °C) > Rh/γ-Al_2O_3 (349 °C) > Pt/γ-Al_2O_3 (361 °C) = Pd/γ-Al_2O_3 (361 °C) > Au/γ-Al_2O_3 (373 °C) > Ir/γ-Al_2O_3 (380 °C). Overall, the Ru-based catalyst showed the best 1,2-DCE degradation performance among the noble metal catalysts, which might be associated with its excellent dechlorination effect from Deacon reaction process [9], and which has the advantage of decreasing the toxic impact of chlorine species compared to other noble metal materials. On the other hand, the simple synthesis method of $NaBH_4$ and hydrazine hydrate reduction could create superior NM-supported catalysts compared with most of the other samples, as shown in Table S1. What is more, the catalytic ability of γ-Al_2O_3 was tested and illustrated in Figure S2, where a 90% 1,2-DCE conversion occurred at 419 °C, the efficiency is far lower than that of noble metal-supported catalysts, indicating that the enhancement of the oxidation ability is mainly ascribed to the participation of noble metals.

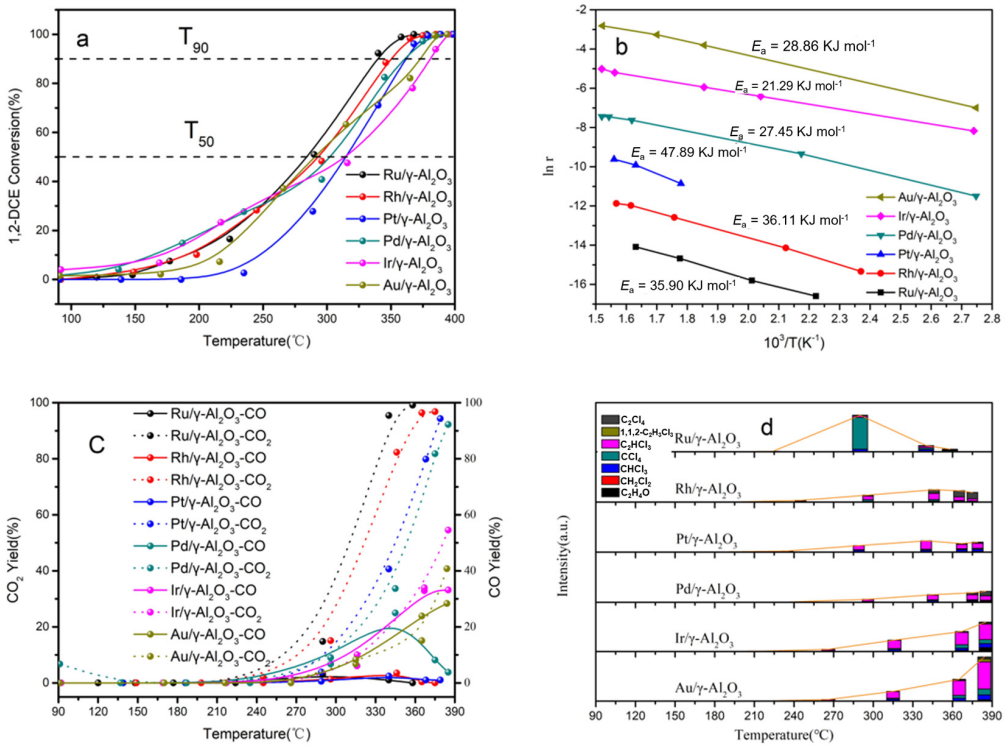

Figure 1. (**a**) 1,2-DCE conversion curves of NM/γ-Al_2O_3 catalysts; (**b**) Arrhenius plots of active samples for 1,2-DCE catalytic oxidation over NM/γ-Al_2O_3 catalysts; (**c**) CO yield and CO_2 yield over NM/γ-Al_2O_3 catalysts; (**d**) Distribution of by-products over NM/γ-Al_2O_3 catalysts during 1,2-DCE oxidation.

The CO and CO_2 yield from effluent streams of the NM/γ-Al_2O_3 catalysts was tested and is displayed in Figure 1c. As shown, the CO_2 yield of NM/γ-Al_2O_3 catalysts enhances with the increase in reaction temperature. Along with the 1,2-DCE complete oxidation condition, the CO_2 yield efficiency of the prepared catalysts can be ordered as follows: Ru/γ-Al_2O_3 (99.15%) > Rh/γ-Al_2O_3 (96.79%) > Pt/γ-Al_2O_3 (94.31%) > Pd/γ-Al_2O_3 (92.20%) > Ir/γ-Al_2O_3 (54.52%) > Au/γ-Al_2O_3 (40.76%). As shown, the CO yield increases along with the climbing temperature and decreases rapidly when 1,2-DCE conversion is more than 50% for Ru/γ-Al_2O_3, Rh/γ-Al_2O_3, Pt/γ-Al_2O_3, and Pd/γ-Al_2O_3 catalysts. Moreover, CO concentration increases with the increase in temperature over Ir/γ-Al_2O_3 and Au/γ-Al_2O_3. In summary, the CO yield of those catalysts at the temperature of 1,2-DCE complete oxidation can be ordered as follows: Ir/γ-Al_2O_3 (33.14%) > Au/γ-Al_2O_3 (28.33%) > Pd/γ-Al_2O_3 (3.81%) > Pt/γ-Al_2O_3 (1.00%) > Rh/γ-Al_2O_3 (0.07%) > Ru/γ-Al_2O_3 (0%). CO_x generation is usually represented as an indicator of mineralization of VOC oxidation; in this aspect, Ru/γ-Al_2O_3 displayed the highest mineralization efficiency compared with other catalysts.

Figure 1b and Table 1 show the E_a tendency of the prepared catalysts, which was calculated to further evaluate the catalytic behavior of the prepared materials. The E_a indexes of the synthesized catalysts can be ordered as follows: Pt/γ-Al_2O_3 (47.89 KJ·mol^{-1}) > Rh/γ-Al_2O_3 (36.11 KJ·mol^{-1})> Ru/γ-Al_2O_3 (35.90 KJ·mol^{-1}) > Au/γ-Al_2O_3 (28.89 KJ·mol^{-1}) > Pd/γ-Al_2O_3 (27.45 KJ·mol^{-1}) > Ir/γ-Al_2O_3 (21.29 KJ·mol^{-1}), suggesting that Ir/γ-Al_2O_3 boasts the lowest light-off temperature and expresses the highest 1,2-DCE conversion activity at low temperatures. At the same time, the TOFs were also estimated at a low conversion efficiency range (200 °C was used in this case) and listed in Table 1. Of course, the TOF value of NM/Al_2O_3 catalysts for 1,2-DCE oxidation at 200 °C can be ordered as follows: Ir/Al_2O_3 > Pd/Al_2O_3 > Ru/Al_2O_3 > Rh/Al_2O_3 > Au/Al_2O_3 > Pt/Al_2O_3, indicating the superior low-temperature activity of the Ir- and Pd-based catalysts and poorest performance of the Pt-based sample. However, a slightly different trend is found with that of E_a, where the Ru- and Rh-based catalysts exhibited higher TOF values compared to that

of Au, which is the opposite of the E_a tendency, suggesting an intrinsic potential activity of Ru/Al_2O_3 and Rh/Al_2O_3 in the 1,2-DCE oxidation reaction [20].

Table 1. Catalytic activity of synthesized catalysts.

Samples	Conversion		E_a [a]	TOF [b]
	T_{50} (°C)	T_{90} (°C)	kJ mol^{-1}	10^{-3} s^{-1}
Ru/γ-Al_2O_3	289	337	30.90	3.19
Rh/γ-Al_2O_3	220	349	36.11	2.89
Pt/γ-Al_2O_3	228	361	35.89	0.84
Pd/γ-Al_2O_3	227	361	27.45	4.75
Au/γ-Al_2O_3	267	373	40.89	2.12
Ir/γ-Al_2O_3	230	380	31.29	7.16

[a] Apparent activation energy: calculated by Equation (6); [b] Turnover frequency: calculated by Equation (7) at 200 °C.

The organic by-products were further evaluated during 1,2-DCE destruction. As shown in Figure 1d, all by-products in the process of 1,2-DCE destruction over the NM/γ-Al_2O_3 catalysts were acetaldehyde (C_2H_4O), dichloromethane (CH_2Cl_2), trichloromethane ($CHCl_3$), tetrachloromethane (CCl_4), trichloroethylene (C_2HCl_3), 1,1,2-trichloroethane (1,1,2-$C_2H_3Cl_3$), and tetrachloroethylene (C_2Cl_4). The amounts of by-products increased gradually with the elevating temperature first, and then decreased slightly with the temperature at 50% conversion of 1,2-DCE over the Ru/γ-Al_2O_3, Rh/γ-Al_2O_3, and Pt/γ-Al_2O_3 catalysts. For the other catalysts, the amounts of by-products increased gradually with the increase in temperature over the Pd/γ-Al_2O_3, Ir/γ-Al_2O_3, and Au/γ-Al_2O_3 catalysts until the highest test temperature of 400 °C. Summarily, the amounts of organic by-products of the prepared catalysts can be ordered as follows: Au/γ-Al_2O_3 > Ir/γ-Al_2O_3 > Pt/γ-Al_2O_3 > Pd/γ-Al_2O_3 > Rh/γ-Al_2O_3 > Ru/γ-Al_2O_3. Along with the analysis of the CO_x yield tendency, it was observed that although the Au- and Ir-based catalysts obtained a higher 1,2-DEC conversion efficiency at lower temperatures, the conversion just stops at the point of "degradation" at higher temperatures, with higher organic compound generation and lower mineralization efficiency. In contrast, a superior "destruction" ability was found for Ru/γ-Al_2O_3, which exhibited the maximum emergence level of organic by-products at 300 °C and then decreased significantly with the increasing temperature, which shows the lowest organic generation under its T_{90} reaction conditions compared with that of other catalysts.

The durability ability of the NM/Al_2O_3 catalysts was also tested for 1,2-DCE catalytic oxidation at each T_{90} condition to evaluate their stability performance. As shown in Figure 2, the Pt, Rh, and Ru catalysts could sustain 90% conversion efficiency in 50 h of operation, while Au, Ir, and Pd could only sustain this level of conversion efficiency for 44, 47, and 40 h, respectively. In summary, Ru/Al_2O_3 exhibited a better long-term operation stability at a lower temperature of 337 °C, with higher mineralization efficiency and lower organic by-product generation, making it more suitable for practical applications compared with other NM/Al_2O_3 catalysts.

3.2. Crystalline and Morphology

Figure S1 shows the XRD pattern of supporting material γ-Al_2O_3, in which the typical diffraction peaks of 2θ at 32.0°, 37.7°, 45.7°, and 66.6° are well agreed with PDF card # 97-003-9014. Figure 3 showed the XRD patterns of all prepared materials. Of course, all NM/γ-Al_2O_3 catalysts have similar diffraction peaks at 2θ = 45.7° and 67.1°, which can be attributed to the presence of γ-Al_2O_3. The Ru/γ-Al_2O_3 catalyst exhibits three obvious diffraction peaks at 2θ of 27.9°, 34.8°, and 54.2°, suggesting the formation of RuO_2 phase [36]. No crystalline phase related to rhodium oxide can be identified with Rh/γ-Al_2O_3, suggesting that the rhodium species exhibits a high level of dispersion on the surficial framework of the γ-Al_2O_3 support [41]. A diffraction peak can be identified at 2θ = 39.7° over Pt/γ-Al_2O_3 catalyst, attributed to the Pt (111) plane of metallic Pt [42].

There are three small diffraction peaks for the Pd/γ-Al_2O_3 catalyst at 2θ = 34.3°, 54.9°, and 61.2°, which can be attributed to the PdO phase [43]. The Ir/γ-Al_2O_3 catalyst exhibits two small diffraction peaks at approximately 35.1° and 53.1°, suggesting the appearance of IrO_2 phase [44]. No crystalline phase can be found for Au/γ-Al_2O_3, which suggests the Au species was dispersed well on the surface of the γ-Al_2O_3 support [45].

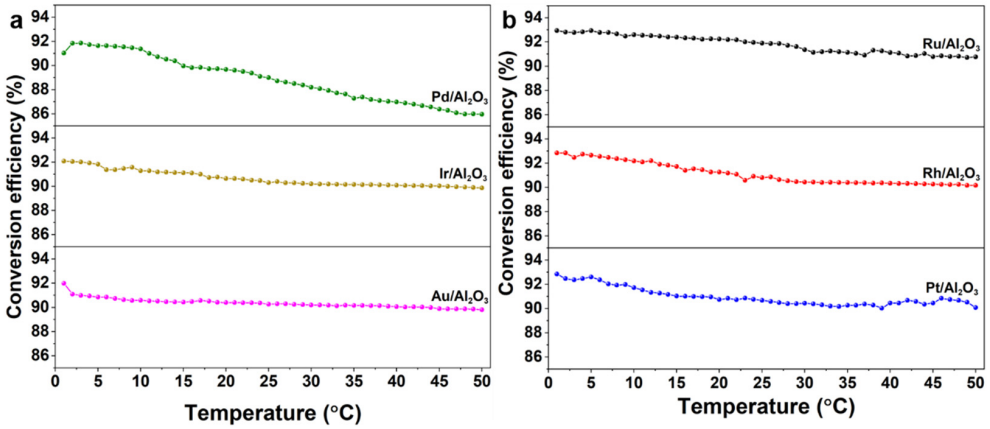

Figure 2. 1,2-DCE conversion curves of (**a**) Au/γ-Al_2O_3, Ir/γ-Al_2O_3, and Pd/γ-Al_2O_3 catalysts and (**b**) Pt/γ-Al_2O_3, Rh/γ-Al_2O_3, Ru/γ-Al_2O_3 catalysts.

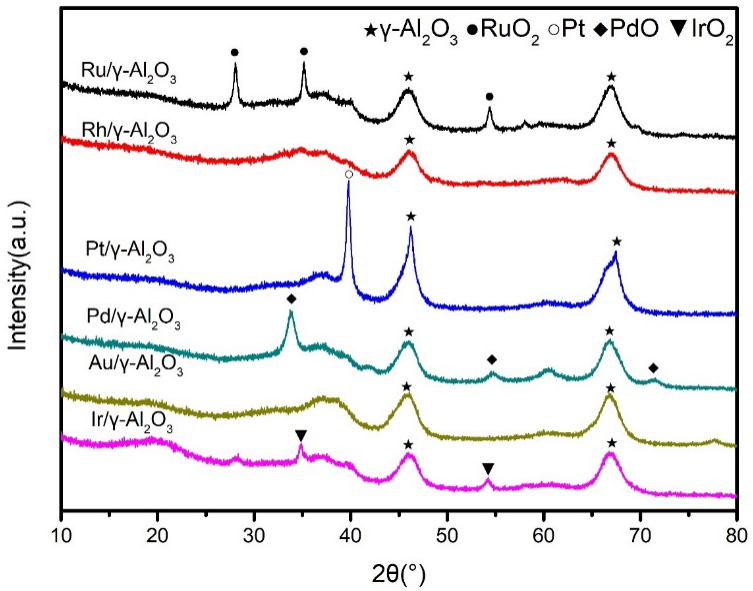

Figure 3. XRD patterns of prepared catalysts.

Figures 4 and 5 show the typical SEM images and the EDS elemental mapping of the prepared samples. As displayed, the FE-SEM photos in Figure 4a,g,m suggest that precious metal species are well-distributed, especially for Rh/γ-Al_2O_3. Meanwhile, Pt/γ-Al_2O_3 and Pd/γ-Al_2O_3 exhibit a slight reunion, which is also reflected by the sharp peak in the XRD patterns. Figure 4d–f,j–l,p–r and Figure 5d–f,j–l,p–r depict the EDS images of all prepared materials. It also can be recognized that Al, O, Ru, Rh, Pt, Pd, Ir, and Au were dispersed homogeneously over each catalyst.

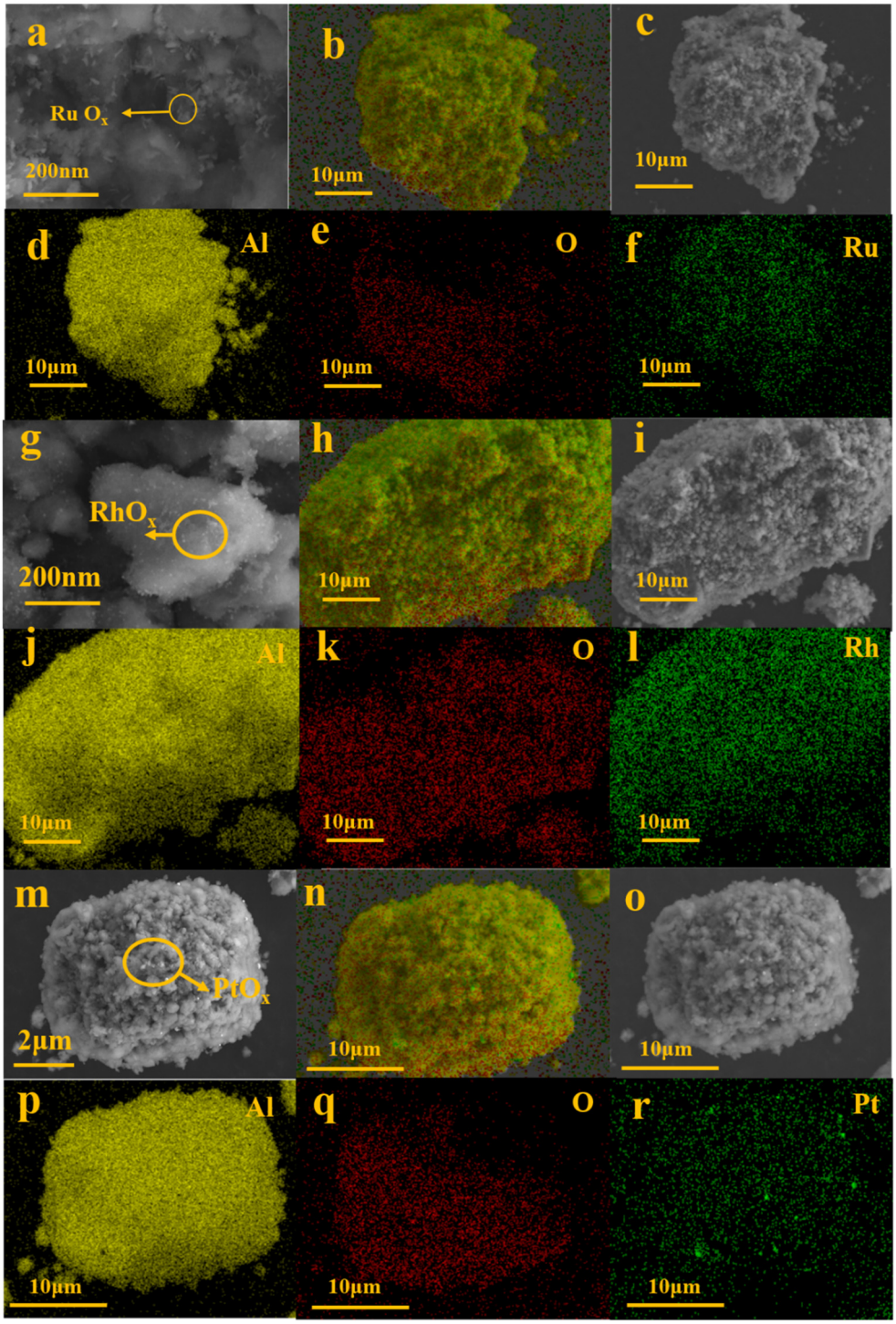

Figure 4. FE-SEM images of (**a**) Ru/γ-Al_2O_3, (**g**) Rh/γ-Al_2O_3, (**m**) Pt/γ-Al_2O_3; EDS elemental mapping of (**b**,**d**–**f**) Ru/γ-Al_2O_3, (**h**,**j**–**l**) Rh/γ-Al_2O_3, (**n**,**p**–**r**) Pt/γ-Al_2O_3 derived from the SEM images of (**c**), (**i**), and (**o**), respectively.

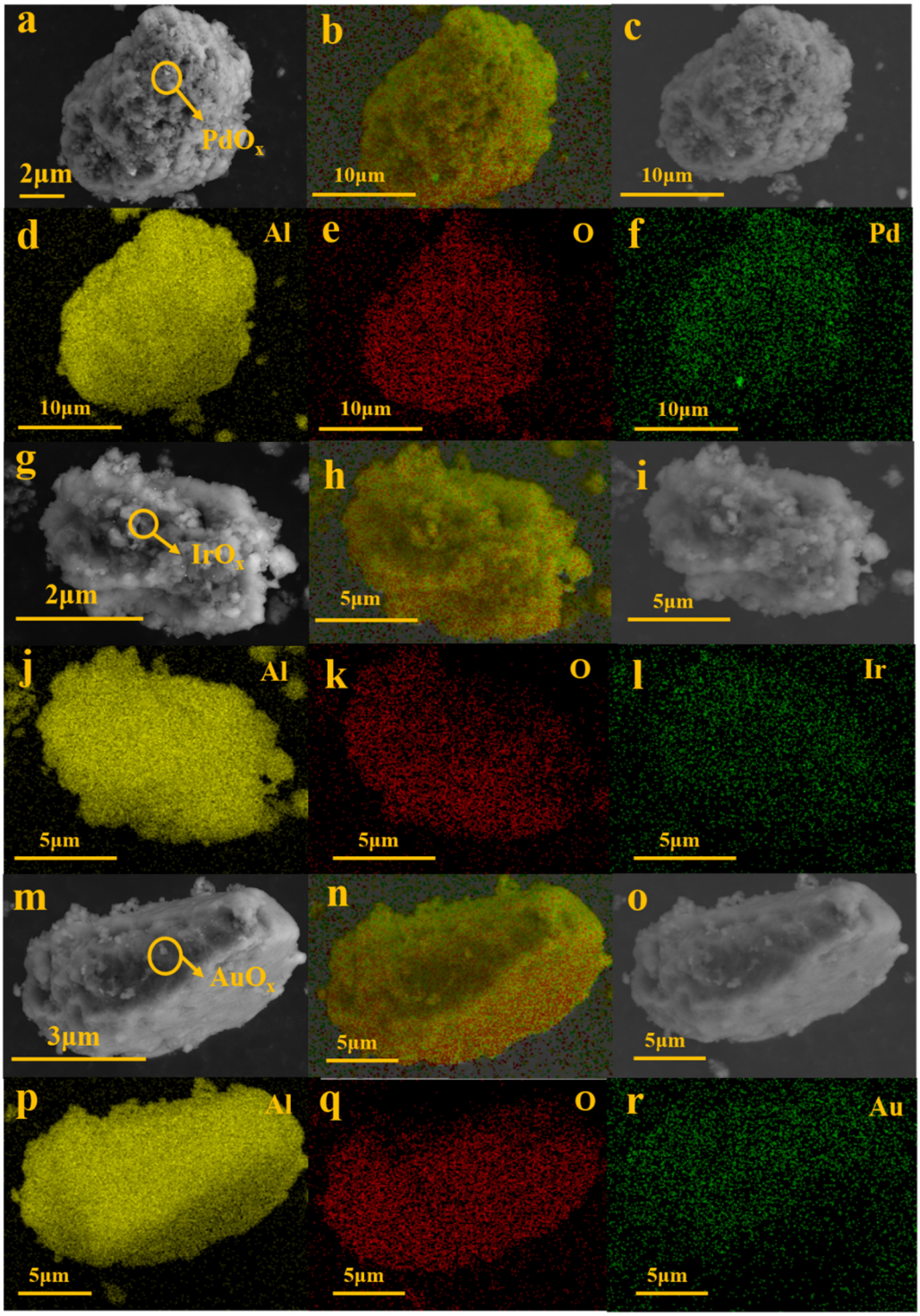

Figure 5. FE-SEM images of (**a**) Pd/γ-Al_2O_3, (**g**) Ir/γ-Al_2O_3, (**m**) Au/γ-Al_2O_3; EDS elemental mapping of (**b**,**d**–**f**) Pd/γ-Al_2O_3, (**h**,**j**–**l**) Ir/γ-Al_2O_3, (**n**,**p**–**r**) Au/γ-Al_2O_3 derived from the SEM images of (**c**), (**i**), and (**o**), respectively.

The textural features of the synthesized samples were evaluated by N_2 physisorption measurements. As expressed in Figure 6a, the adsorption-desorption isotherm curves of all prepared catalysts are type IV [46], which forms a closed loop with the previous adsorption curve at medium pressure. After analyzing the BET surface areas (Table 2) of the prepared catalysts, the values could be ordered as follows: Au/γ-Al_2O_3 (266.79 $m^2 \cdot g^{-1}$) > Ir/γ-Al_2O_3 (230.35 $m^2 \cdot g^{-1}$) > Ru/γ-Al_2O_3 (229.27 $m^2 \cdot g^{-1}$) > Pt/γ-Al_2O_3 (227.60 $m^2 \cdot g^{-1}$)

> Pd/γ-Al_2O_3 (226.79 $m^2 \cdot g^{-1}$) > Rh/γ-Al_2O_3 (219.97 $m^2 \cdot g^{-1}$) > γ-Al_2O_3 (207.87 $m^2 \cdot g^{-1}$). Moreover, in terms of pore volume, the catalysts can be ordered as follows: Pt/γ-Al_2O_3 (0.813 $cm^3 \cdot g^{-1}$) > Rh/γ-Al_2O_3 (0.595 $cm^3 \cdot g^{-1}$) > Au/γ-Al_2O_3 (0.589 $cm^3 \cdot g^{-1}$) > Ir/γ-Al_2O_3 (0.510 $cm^3 \cdot g^{-1}$) > Pd/γ-Al_2O_3 (0.502 $cm^3 \cdot g^{-1}$) > Ru/γ-Al_2O_3 (0.468 $cm^3 \cdot g^{-1}$) > γ-Al_2O_3 (0.436 $cm^3 \cdot g^{-1}$). Generally, a large pore volume is conducive to exposing more active sites, which would be profitable for reactant capture and for improving the anti-carbon deposition ability of the catalyst. As depicted in Figure 6b, the most probable pore sizes of all prepared materials were distributed between 2 and 4 nm, combining the existence hysteresis loop between a P/P_0 of 0.6 and 0.8, suggesting the occurrence of a mesoporous structure.

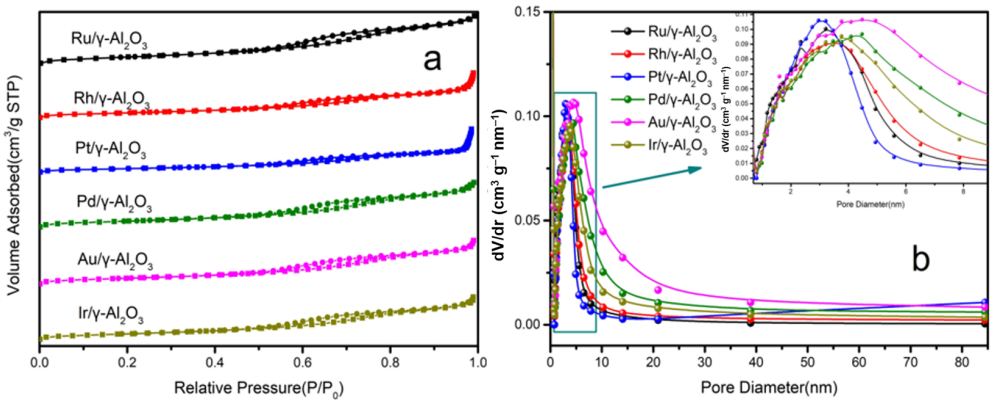

Figure 6. (**a**) N_2 adsorption-desorption isotherms curves and (**b**) Pore size distribution of all prepared catalysts.

Table 2. Physicochemical properties of synthesized catalysts.

Samples	S_{BET} [a] $m^2 \cdot g^{-1}$	V [b] $cm^3 \cdot g^{-1}$	D_p [c] nm	Loading [d] %	*D* (NM Dispersion) [e] %
γ-Al_2O_3	207.87	0.436	4.20	/	/
Ru/γ-Al_2O_3	229.29	0.468	4.09	0.97	31.1
Rh/γ-Al_2O_3	219.97	0.595	5.41	0.98	27.4
Pt/γ-Al_2O_3	227.60	0.813	7.14	1.01	25.6
Pd/γ-Al_2O_3	226.79	0.502	4.43	1.02	29.7
Au/γ-Al_2O_3	266.62	0.589	4.42	0.96	40.2
Ir/γ-Al_2O_3	230.35	0.510	4.43	0.96	33.5

[a] Specific surface area based on the calculation of P/P_0 = 0.05–0.30; [b] Total pore volume tested at P/P_0 = 0.99; [c] BJH pore size calculated from the N_2 desorption branch; [d] Weight loading of noble metals of prepared materials tested by ICP-OES; [e] Calculated from CO chemisorption measurements using average CO:NM stoichiometry of 1:1; *D* (%) = $N_{surface}$ of NM/N_{total} of NM.

3.3. Catalyst Reducibility, Acid Properties, and Oxygen Species

The redox characteristics of the as-prepared catalysts were determined by H_2-TPR experiments. First of all, an H_2-TPR pattern of the supporting material γ-Al_2O_3 is shown in Figure 7a, where no obvious H_2 consumption appeared for γ-Al_2O_3, with the exception of a small peak centered at 735 °C, demonstrating the poor reduction properties of the supporting material γ-Al_2O_3. For all supported noble metal-based catalysts in this work, the low-temperature range peaks could be recognized as a noble metal reduction action. For instance, a sharp peak located at about 153 °C in the Ru/γ-Al_2O_3 profile resulted from the reduction of Ru^{4+} to Ru^0. As for the Rh/γ-Al_2O_3 sample, the reduction peak at the temperature range 78 °C was related to the reduction of Rh^{3+} to Rh^+, but then the

second emergence peak centered at 286 °C was caused by the reduction of Rh^{+} to Rh^{0}. The hydride consumption spike at the temperature of 473 °C for the Pt/γ-Al_2O_3 catalyst can be attributed to the transformation of Pt^{2+} to Pt^{0}. Interestingly, a negative peak occurred at about 44 °C and can be observed for the Pd/γ-Al_2O_3 material; this represents the decomposition of palladium hydrides [47] due to the superior hydrogen storage capacity of Pd, which might generate partial palladium hydrides during the hydrazine hydrate treatment process. Moreover, the peak centered at 428 °C resulted from the reduction of Pd^{2+} to Pd^{0}. For the Ir/γ-Al_2O_3 material, the reduction peak at 199 °C corresponded to the reduction of Ir^{3+} to Ir^{+}, and the following peak located at 417 °C can be attributed to the reduction of Ir^{+} to Ir^{0}. There is no obvious reduction peak in the profile of the Au/γ-Al_2O_3 catalyst, which corresponded to the redox properties of the Au metal. The reduction procedures of the prepared materials result from electron transfer among different metal compositions, which would promote the reaction rate of 1,2-DCE oxidation.

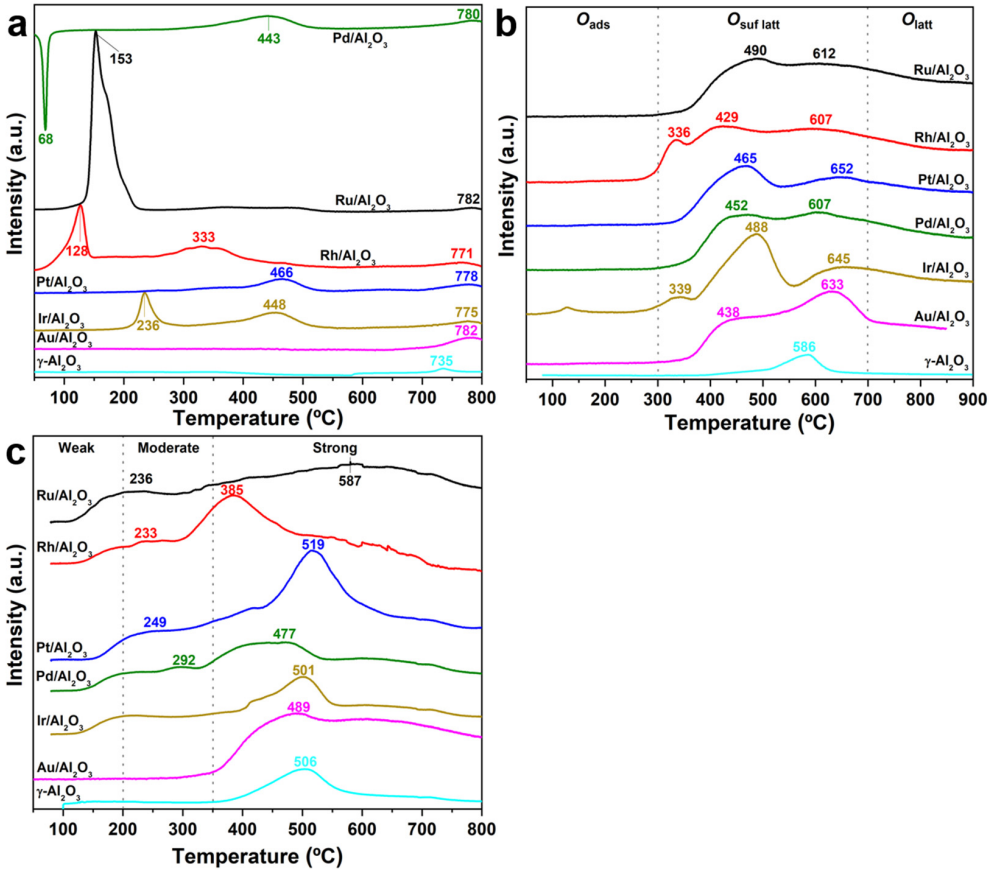

Figure 7. (**a**) H_2-TPR, (**b**) O_2-TPD, and (**c**) NH_3-TPD profiles of all prepared catalysts.

In a typical oxidation process, the acid property of the catalysts is another important influencing factor for the 1,2-DCE reaction [48,49]. The surface acidity of the prepared samples was investigated by NH_3-TPD measurement, and the resulting profiles are exhibited in Figure 7c. Across all catalysts, the acidic sites identified from the NH_3-TPD patterns can be classified into three categories, namely, those containing weak acidity (<200 °C), those with moderate acidity (200–350 °C), and those with strong acidity (>350 °C) [38,50–52]. For the supporting material γ-Al_2O_3, only one significant peak at 506 °C was observed, indicating that γ-Al_2O_3 belongs to the strong acidity category. When supporting noble metals, the desorption of the strong acidity range of Pt/γ-Al_2O_3 was strengthened significantly, and the Au-, Ir-, and Pd-based materials were also increased extensively. Interestingly, the desorption peaks in the moderate and weak acid ranges emerged in all NM/γ-Al_2O_3 catalysts, especially in those with moderate acidity, suggesting the possible existence of Brønsted

acid sites, where Ru/γ-Al_2O_3 was observed to exhibit more moderate acid emergence than other samples. Strong acid sites generally refer to Lewis acid sites [41]; 1,2-DCE is usually easily trapped on Lewis acid sites, causing the dehydrochlorination effect and inducing the formation of the main by-product (vinyl chloride). On the other hand, the Brønsted acid sites can efficiently promote the desorption of chlorine species from the catalyst surface, further relieving the chlorination effect during 1,2-DCE degradation, as well as hindering the formation of chlorine by-products [25]. As a result, the intensive nature of Brønsted acid sites and the suitable amount of Lewis acid sites may contribute to the excellent performance of Ru/γ-Al_2O_3 in 1,2-DCE destruction.

Moreover, O_2-TPD was carried out for the determination of the oxygen species (which can be generally divided into three types [53,54]), as displayed in Figure 7b: the desorption of oxygen species at low temperature < 300 °C can be associated with surface physically adsorbed oxygen ($O_{2(ad)}$) and surface chemically adsorbed oxygen ($O_2^-{}_{(ad)}$, $O^-{}_{(ad)}$). On the other hand, the middle-temperature emergence of desorption peaks in the range of 300 and 700 °C can be attributed to surface lattice oxygen ($O^{2-}{}_{(ad)}$). Finally, the adsorption peak overcrossing higher temperature (> 700 °C) regions may be related to the lattice oxygen (O^{2-}) of the bulk phase. It is shown that only a weak desorption peak at 503 °C emerged for γ-Al_2O_3, which is likely associated with the surface lattice oxygen species. When supporting noble metals, for all the prepared materials, there is no adsorption peak in the low- and high-temperature ranges, but only at the temperature range 300–700 °C, which indicates that surface lattice oxygen represents the main oxygen species in noble metal-based catalysts. In addition, the evolution processes of oxygen species usually convert following the procedures $O_{2(ad)} \rightarrow O_2^-{}_{(ad)} \rightarrow O^-{}_{(ad)} \rightarrow O^{2-}{}_{(lattice)}$ [55], while the adsorbed oxygen changes for all prepared catalysts in the following manner $O_{2(ad)} \rightarrow O_2^-{}_{(ad)} \rightarrow O^-{}_{(ad)}$, which is attributed to the influence of precious metal oxide species. Moreover, as compared with the support γ-Al_2O_3, all noble metal catalysts showed an obvious increasing desorption amount in the temperature region of 300–700 °C, as well as a significant low-temperature shift in oxygen desorption, suggesting a promotion of active oxygen and oxygen mobility. By combining other characterization methods, the presence of noble metals in all prepared catalysts strengthens significantly the mobility of oxygen adsorbed on the surface of the materials.

This section may be divided into subheadings. It aims to provide a concise and precise description of the experimental results and interpretations of them, as well as the experimental conclusions that can be drawn.

3.4. Catalyst Surface Status

The information on the element composition, the metallic valence status, and oxygen species on the surface of samples can be analyzed by XPS measurement, where O 1*s*, Ru 3*p*, Rh 3*d*, Pt 4*f*, Pd 3*d*, Ir 4*f*, and Au 4*f* were analyzed and are shown in Figures 8 and 9. For all supported noble metal catalysts, as illustrated in Figure 8, O 1*s* patterns could be categorized into two types: the one with a binding energy (BE) of ~529.8 eV may be related to lattice oxygen species (O^α), while the other one centered at 531.5 eV belongs to the surface adsorbed oxygen species (O^β), respectively [56]. The $O^\alpha/(O^\alpha + O^\beta)$ ratio by Gauss fitting is listed in Table 3, and allows for the ordering of the catalysts as follows: Ru/γ-Al_2O_3 (0.88) > Au/γ-Al_2O_3 (0.86) > Ir/γ-Al_2O_3 (0.85) > Pt/γ-Al_2O_3 (0.82) > Rh/γ-Al_2O_3 (0.81) > Pd/γ-Al_2O_3 (0.68).

For the noble metal XPS patterns, the Ru 3*p* spectra of Ru/γ-Al_2O_3 could be fitted into two obvious peaks, where the BEs of 496.6 and 463.6 eV are attributed to the surface Ru^{4+} species [57]. The Rh 3*d* spectrum of Rh/γ-Al_2O_3 includes two BE combinations of 308.6 and 313.4 eV, which means the Rh^{3+} species are present on the surface [58]. The Pt 4*f* spectrum of the Pt/γ-Al_2O_3 catalyst showed doublet peaks with BEs of 75.1 and 71.5 eV; these belong to the surface Pt^{2+} species [25]. The Pd 3*d* spectra included two peaks at 336.6 and 342.6 eV both associated with Pd^{2+} species [37]. In the Ir 4*f* spectrum, the peaks can be identified as $4f_{5/2}$ (BEs ≈ 64.5 eV) and Ir $4f_{7/2}$ (BEs ≈ 62.0 eV), respectively, confirming

the existence of Ir^{3+} species on the surface [44]. Two peaks assigned to Au 4*f* at BEs of 88.1 and 84.2 eV were associated with the surface Au^{+} species [45]. Abundant adsorbed oxygen concentration on the catalyst surface as well as a higher noble metal valence are conducive to improving oxidation behavior, which plays a key role in the catalytic oxidation process of noble metal catalysts [54].t

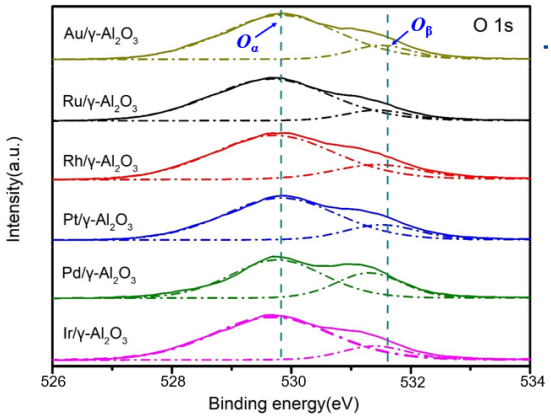

Figure 8. O 1*s* spectra of all prepared noble metal-based catalysts.

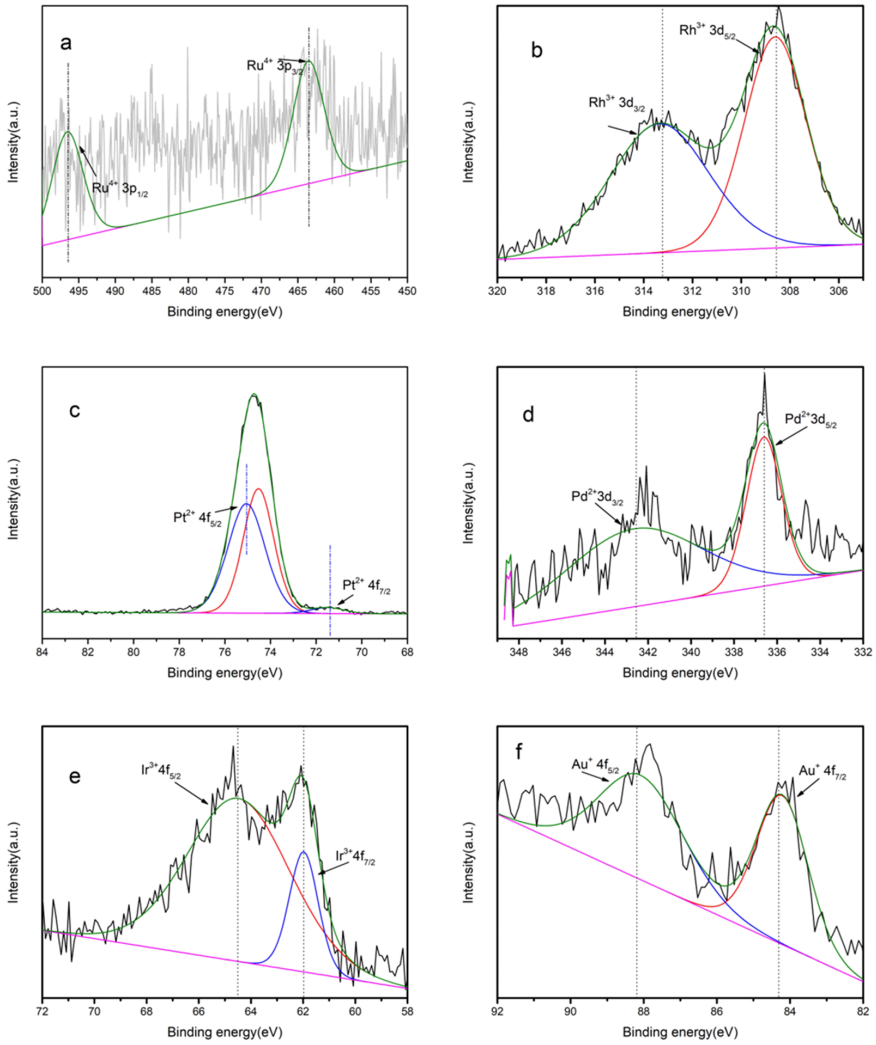

Figure 9. Ru 3*p*, Rh 3*d*, Pt 4*f*, Pd 3*d*, Ir 4*f*, Au 4*f* spectra of (**a**) Ru/γ-Al_2O_3, (**b**) Rh/γ-Al_2O_3, (**c**) Pt/γ-Al_2O_3, (**d**) Pd/γ-Al_2O_3, (**e**) Ir/γ-Al_2O_3, (**f**) Au/γ-Al_2O_3 catalysts.

Table 3. XPS results of O 1s of prepared catalysts.

Samples	O 1*s*		
	O_α [a]	O_β [b]	$O_\alpha/(O_\alpha + O_\beta)$
Ru/γ-Al_2O_3	53,918.9	7038.0	0.88
Rh/γ-Al_2O_3	48,460.7	11,390.2	0.81
Pt/γ-Al_2O_3	38,974.4	8706.5	0.82
Pd/γ-Al_2O_3	25,771.9	11,941.7	0.68
Ir/γ-Al_2O_3	41,634.6	7145.6	0.85
Au/γ-Al_2O_3	46,326.8	7463.6	0.86

[a] Lattice oxygen species; [b] Surface adsorbed oxygen species.

3.5. Catalyst Intermediate Species and Oxidation Mechanisms

Two typical kinetic models of the oxidation mechanisms of 1,2-DCE over noble metal catalysts as displayed in Scheme 1. In the low-temperature region, the oxidation mechanism of 1,2-DCE on noble metal catalysts obeys the Langmuir-Hinshelwood model: (1) 1,2-DCE and the oxygen species are simultaneously adsorbed onto the surficial active sites; (2) 1,2-DCE molecules react with the adsorbed oxygen and then produce Cl_2, H_2O, HCl, and CO_2; (3) intermediates continuously react with the adsorbed oxygen and generate H_2O, CO_2, HCl, and Cl_2. On the other hand, at high temperatures, the 1,2-DCE oxidation routes of the NM/γ-Al_2O_3 catalysts follow the Eley-Rideal model [29]: (1) oxygen species are adsorbed; (2) the adsorbed oxygen species further react with the gas-phase 1,2-DCE to produce H_2O, HCl, Cl_2, and CO_2. In summary, the surface-adsorbed oxygen species are the main source of 1,2-DCE oxidation.

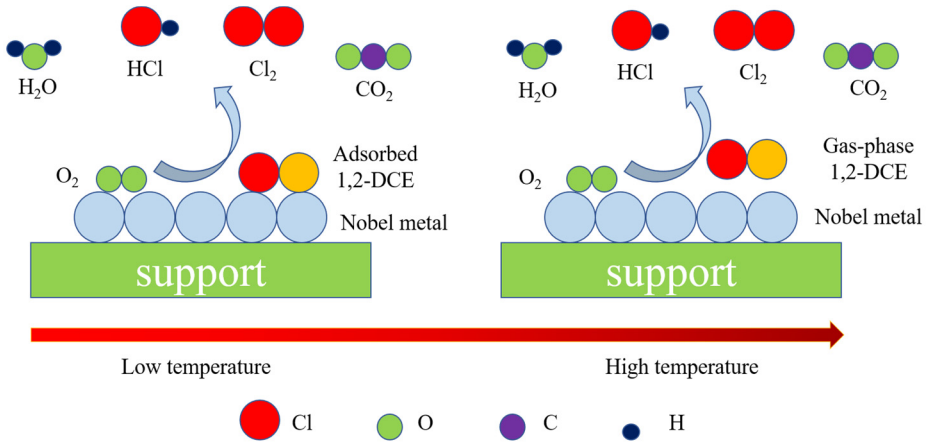

Scheme 1. 1,2-DCE oxidation routes in two typical kinetic models of supported noble metal catalysts (Langmuir-Hinshelwood model and Eley-Rideal model).

By combining other characterization methods and the by-product distribution, four reaction paths can be inferred, as displayed in Scheme 2 [40,59]. Path 1: 1,2-DCE induces the dehydrochlorination reaction to produce vinyl chloride; vinyl chloride reacts with H· to generate carbon dioxide positive ions; carbon dioxide positive ions react with O^{2-} to create acetate. Path 2: vinyl chloride reacts with chlorine to produce trichloroethane; trichloroethylene can be generated by trichloroethane reacting with chlorine and the dehydrochlorination reaction. Path 3: 1,2-DCE induces C-C bond cleavage to create chloromethane; chloromethane reacts with H^+ and O^{2-} to produce formate. Path 4: chloromethane reacts with chlorine in the dehydrochlorination reaction to generate dichloromethane; dichloromethane reacts with chlorine in the dehydrochlorination reaction to create trichloromethane; trichloromethane reacts with chlorine in the dehydrochlorination reaction to produce carbon tetrachloride. Finally, these intermediates are then deeply oxidized into H_2O, HCl, Cl_2, and CO_2.

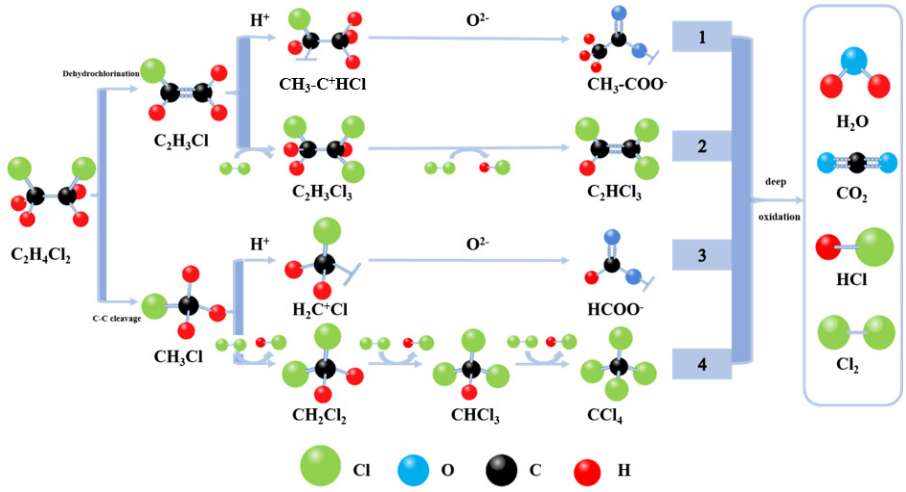

Scheme 2. Proposed 1,2-DCE oxidation mechanism of prepared catalysts.

To further explore the oxidation mechanisms of the 1,2-DCE catalyst over noble metals, *in situ* DRIFTS measurements were applied to discover the reaction intermediates of all catalyst materials when 1,2-DCE degrades from 90 to 260 °C (Figure 10). All of the catalysts could be observed in the bands in the region of 3550–3060 cm^{-1}, which are determined by the -OH vibration with surficial adsorbed water. Of course, with the elevated operation temperature, the strength of these bands is reduced contrarily. Following the stretching vibration of the C-H band observed in the bands of 2930 and 2850 cm^{-1}, the vibration of the -CH_2 group can be distinguished. At the same time, the C-H vibration appeared at 2820 and 2720 cm^{-1}, indicating the emergence of the -CH_3 group. Moreover, the bands in the region of 1544–1371cm^{-1} are also associated with C-H vibration, which is attributed to the oscillation of -CH/-CH_2/-CH_3 radicals. An overcrossing band at 2360–2340 cm^{-1}, growing in intensity alongside the reaction temperature, is ascribed to the stretching vibration of C=O. Meanwhile, the bands at 1680–1640 cm^{-1} are associated with the stretching vibration of the C=C bond, which indicates the appearance of the banding vibrations of alkene. The band located at 1378 cm^{-1} belongs to the COO- of acetate species, while the one located at 1338 cm^{-1} is associated with the COO- of formate species. The bands at 1250–1000 cm^{-1} can be ascribed to the stretching oscillation of the C-C of 1,2-DCE.

In conclusion, the reaction path of 1,2-DCE over the prepared noble metal-based catalysts could be conducted in several of the main reaction routes of these typical noble metal materials. First, the vibration of C-H (-CH/-CH_2/-CH_3 groups), COO- (acetate), and C=C (alkene) can be found in the Ru/γ-Al_2O_3 sample, and thus the main reaction paths of the Ru/γ-Al_2O_3 catalyst are reaction paths 1 and 4. The vibration of COO- (acetate), C-H (-CH/-CH_2/-CH_3 groups), and C=C (alkene) can be observed for the Rh/γ-Al_2O_3 material, and thus the main reaction paths of the Rh/γ-Al_2O_3 material are reaction paths 1 and 3. In the Pt/γ-Al_2O_3 catalyst spectrum, the vibrations of C-H (-CH_2 group), C-H (-CH/-CH_2/-CH_3 groups), COO- (acetate), and C=C (alkene) are obvious, and thus the reaction paths 1, 2, and 4 are the main reaction paths of Pt/γ-Al_2O_3 material. The vibration of C-H (-CH/-CH_2/-CH_3 groups), COO- (acetate), and C=C (alkene) can be found with the Pd/γ-Al_2O_3 catalyst, so reaction paths 1 and 2 can be observed from the process of Pd/γ-Al_2O_3 material. The vibration of C-H (-CH_2 group), C-H (-CH/-CH_2/-CH_3 group), COO- (acetate), and C=C (alkene) can be observed on the Ir/γ-Al_2O_3 material surface. The vibration of C-H (-CH_2 group), C-H (-CH/-CH_2/-CH_3 groups), COO- (acetate), and C=C (alkene) can be observed on the Au/γ-Al_2O_3 material surface. Finally, the catalyst of Ir/γ-Al_2O_3 follows reaction paths 1, 2, and 4, as does Au/γ-Al_2O_3.

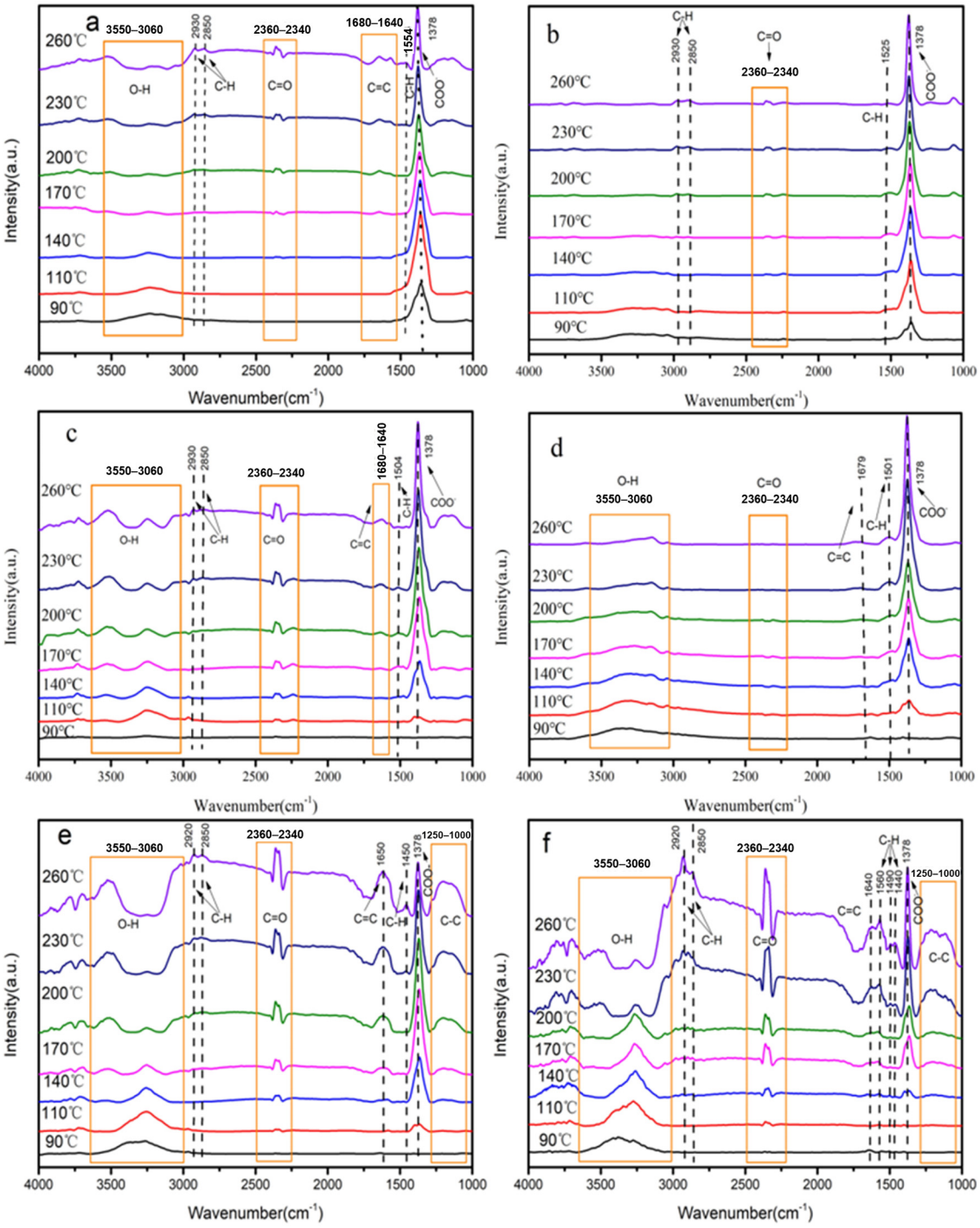

Figure 10. *In situ* DRIFTS spectra of 1,2-DCE catalytic oxidation over (**a**) Ru/γ-Al_2O_3, (**b**) Rh/γ-Al_2O_3, (**c**) Pt/γ-Al_2O_3, (**d**) Pd/γ-Al_2O_3, (**e**) Ir/γ-Al_2O_3, (**f**) Au/γ-Al_2O_3 catalysts.

4. Conclusions

In this work, Al_2O_3 supported a series of precious metals; Ru, Rh, Pt, Pd, Ir, and Au catalysts were prepared with mesopores (pore sizes distributed at 2–4 nm) and all were proven to be able to totally destruct 1,2-DCE below 400 °C. The results suggest that noble metals with high-valence states and superior mobility of surface-adsorbed oxygen species are favorable for 1,2-DCE degradation. To summarize the oxidation procedure, 1,2-DCE is first captured by the surficial active sites and then activated, and oxidized into intermediate products (such as vinyl chloride, acetate, trichloroethane, trichloroethylene, dichloromethane, trichloromethane, tetrachloromethane, and trichloroethylene), before the

products are deeply oxidized to form H_2O, CO_2, HCl, and Cl_2, which suggests that the prepared materials had a high-valence state and abundant active oxygen species, making them promising candidates for CVOC destruction. This work supplies a systematical comparison study of various typical noble metal catalysts with an exploration of the potential for CVOC destruction.

Supplementary Materials: Following supporting information can be downloaded at: https://www.mdpi.com/article/10.3390/app13010036/s1, Figure S1: XRD pattern of original supporting material γ-Al_2O_3; Figure S2: 1,2-DCE conversion curves of original supporting material γ-Al_2O_3; Text S1: Characterization method; Text S2: *In situ* DRIFTS. Refs. [22,23,25,30,32,34,36,60–62] are cited in Supplementary file.

Author Contributions: L.L.: Investigation, Data curation, Visualization, Writing-original draft, Funding acquisition; J.Z.: Software, Supervision, writing-review and editing; H.X.: Investigation, Validation, Methodology; M.T. and C.H.: Resources, Project administration, Supervision, Writing-review and editing. All authors have read and agreed to the published version of the manuscript.

Funding: This work is appreciated the financial support from the National Natural Science Foundation of China (22106124 and 22276145), Natural Science Foundation of Shaanxi Province (2021JQ-011).

Institutional Review Board Statement: Not applicable.

Informed Consent Statement: Not applicable.

Data Availability Statement: Not applicable.

Acknowledgments: This work is appreciated the financial support from the National Natural Science Foundation of China (22106124 and 22276145), Natural Science Foundation of Shaanxi Province (2021JQ-011), and Instrumental Analysis Center of Xi'an Jiaotong University.

Conflicts of Interest: The authors declare no conflict of interest.

References

1. He, C.; Cheng, J.; Zhang, X.; Douthwaite, M.; Pattisson, S.; Hao, Z.P. Recent Advances in the catalytic oxidation of volatile organic compounds: A review based on pollutant sorts and sources. *Chem. Rev.* **2019**, *119*, 4471–4568. [CrossRef] [PubMed]
2. Dumanoglu, Y.; Kara, M.; Altiok, H.; Odabasi, M.; Elbir, T.; Bayram, A. Spatial and seasonal variation and source apportionment of volatile organic compounds (VOCs) in a heavily industrialized region. *Atmos. Environ.* **2014**, *98*, 168–178. [CrossRef]
3. Aranzabal, A.; Pereda-Ayo, B.; Gonzalez-Marcos, M.P.; Gonzalez-Marcos, J.A.; Lopez-Fonseca, R.; Gonzalez-Velasco, J.R. State of the art in catalytic oxidation of chlorinated volatile organic compounds. *Chem. Pap.* **2014**, *68*, 1169–1186. [CrossRef]
4. Dai, C.H.; Zhou, Y.Y.; Peng, H.; Huang, S.J.; Qin, P.F.; Zhang, J.C.; Yang, Y.; Luo, L.; Zhang, X.S. Current progress in remediation of chlorinated volatile organic compounds: A review. *J. Ind. Eng. Chem.* **2018**, *62*, 106–119. [CrossRef]
5. Huang, B.; Lei, C.; Wei, C.; Zeng, G. Chlorinated volatile organic compounds (Cl-VOCs) in environment-sources, potential human health impacts, and current remediation technologies. *Environ. Int.* **2014**, *71*, 118–138. [CrossRef]
6. Justicia-Leon, S.D.; Higgins, S.; Mack, E.E.; Griffiths, D.R.; Tang, S.; Edwards, E.A.; Loffler, F.E. Bioaugmentation with distinct Dehalobacter strains achieves chloroform detoxification in microcosms. *Environ. Sci. Technol.* **2014**, *48*, 1851–1858. [CrossRef]
7. Agarwal, S.K.; Spivey, J.J.; Butt, J.B. Catalyst deactivation during deep oxidation of chlorohydrocarbons. *Appl. Catal. A Gen.* **1992**, *82*, 259–275. [CrossRef]
8. Maness, A.D.; Bowman, K.S.; Yan, J.; Rainey, F.A.; Moe, W.M. Dehalogenimonas spp. can Reductively Dehalogenate High Concentrations of 1,2-Dichloroethane, 1,2-Dichloropropane, and 1,1,2-Trichloroethane. *AMB Express* **2012**, *2*, 54. [CrossRef]
9. Du, C.; Lu, S.; Wang, Q.; Buekens, A.G.; Ni, M.; Debecker, D.P. A review on catalytic oxidation of chloroaromatics from flue gas. *Chem. Eng. J.* **2018**, *334*, 519–544. [CrossRef]
10. Beamer, P.I.; Luik, C.; Abrell, L.; Campos, S.; Martínez, M.; Saez, A.E. Concentration of trichloroethylene in breast milk and household water from Nogales, Arizona. *Environ. Sci. Technol.* **2012**, *46*, 9055–9061. [CrossRef]
11. Li, L.; Shi, J.W.; Tian, M.J.; Chen, C.W.; Wang, B.R.; Ma, M.D.; He, C. In situ fabrication of robust three dimensional ordered macroporous γ-MnO_2/$LaMnO_{3.15}$ catalyst for chlorobenzene efficient destruction. *Appl. Catal. B Environ.* **2021**, *282*, 119565. [CrossRef]
12. Pires, J.; Carvalho, A.; Carvalho, M.J.M.; Materials, M. Adsorption of volatile organic compounds in Y zeolites and pillared clays. *Micropor. Mesopor. Mater.* **2001**, *43*, 277–287. [CrossRef]
13. Moon, H.S.; Kim, I.S.; Kang, S.J.; Ryu, S.K. Adsorption of volatile organic compounds using activated carbon fiber filter in the automobiles. *Carbon Lett.* **2014**, *15*, 203–209. [CrossRef]

14. Lemus, J.; Martin-Martinez, M.; Palomar, J.; Gomez-Sainero, L.; Gilarranz, M.A.; Rodriguez, J.J. Removal of chlorinated organic volatile compounds by gas phase adsorption with activated carbon. *Chem. Eng. J.* **2012**, *211–212*, 246–254. [CrossRef]
15. Cloirec, P.L. Treatments of polluted emissions from incinerator gases: A succinct review. *Rev. Environ. Sci. Bio/Technol.* **2012**, *11*, 381–392. [CrossRef]
16. Ryding, J.M.; Puhakka, J.A.; Strand, S.E.; Ferguson, J.F. Degradation of chlorinated phenols by a toluene enriched microbial culture. *Water Res.* **1994**, *28*, 1897–1906. [CrossRef]
17. Lu, S.Y.; Wang, Q.L.; Buekens, A.G.; Yan, J.H.; Li, X.D.; Cen, K.F. Photocatalytic decomposition of gaseous 1,2-dichlorobenzene on TiO_2 films: Effect of ozone addition. *Chem. Eng. J.* **2012**, *195–196*, 233–240. [CrossRef]
18. Huang, H.; Dai, Q.; Wang, X. Morphology effect of Ru/CeO_2 catalysts for the catalytic combustion of chlorobenzene. *Appl. Catal. B Environ.* **2014**, *158–159*, 96–105. [CrossRef]
19. Hu, P.; Huang, H.; Chen, J.; Ye, X.; Leung, D.C. Highly dispersed and active supported Pt nanoparticles for gaseous formaldehyde oxidation: Influence of particle size. *Chem. Eng. J.* **2014**, *252*, 320–326.
20. Sekizawa, K.; Widjaja, H.; Maeda, S.; Ozawa, Y.; Eguchi, K. Low temperature oxidation of methane over Pd/SnO_2 catalyst. *Appl. Catal. A Gen.* **2000**, *200*, 211–217. [CrossRef]
21. Jeong, H.; Lee, G.; Kim, B.; Bae, J.; Han, J.w.; Lee, H. Fully dispersed Rh ensemble catalyst to enhance low-temperature activity. *J. Am. Chem. Soc.* **2018**, *140*, 9558–9565. [CrossRef] [PubMed]
22. Pitkäaho, S.; Matejova, L.; Ojala, S.; Gaalova, J.; Keiski, R.L. Oxidation of perchloroethylene—Activity and selectivity of Pt, Pd, Rh, and V_2O_5 catalysts supported on Al_2O_3, Al_2O_3-TiO_2 and Al_2O_3-CeO_2. *Appl. Catal. B Environ.* **2012**, *113–114*, 150–159. [CrossRef]
23. Maupin, I.; Pinard, L.; Mijoin, J.; Magnoux, P. Bifunctional mechanism of dichloromethane oxidation over Pt/Al_2O_3: CH_2Cl_2 disproportionation over alumina and oxidation over platinum. *J. Catal.* **2012**, *291*, 104–109. [CrossRef]
24. Fornasiero, P.; Dimonte, R.; Rao, G.R.; Kaspar, J.; Meriani, S.; Trovarelli, A.; Graziani, M. Rh-loaded CeO_2-ZrO_2 solid solutions as highly efficient oxygen exchangers: Dependence of the reduction behavior and the oxygen storage capacity on the structural properties. *J. Catal.* **1995**, *151*, 168–177. [CrossRef]
25. Cao, S.; Fei, X.; Wen, Y.; Sun, Z.; Wang, H.; Wu, Z. Bimodal mesoporous TiO_2 supported Pt, Pd and Ru catalysts and their catalytic performance and deactivation mechanism for catalytic combustion of Dichloromethane (CH_2Cl_2). *Appl. Catal. A Gen.* **2018**, *550*, 20–27. [CrossRef]
26. Liang, Y.; Li, J.; He, Y.; Jiang, Z.; Shangguan, W. Catalytic oxidation of dimethyl phthalate over titania-supported noble metal catalysts. *J. Hazard. Mater.* **2020**, *401*, 123274. [CrossRef]
27. He, C.; Li, J.; Li, P.; Cheng, J.; Hao, Z.; Xu, Z.P. Comprehensive investigation of Pd/ZSM-5/MCM-48 composite catalysts with enhanced activity and stability for benzene oxidation. *Appl. Catal. B Environ.* **2010**, *96*, 466–475. [CrossRef]
28. Sinquin, G.; Petit, C.; Libs, S.; Hindermann, J.P.; Kiennemann, A. Catalytic destruction of chlorinated C_1 volatile organic compounds (CVOCs) reactivity, oxidation and hydrolysis mechanisms. *Appl. Catal. B Environ.* **2000**, *27*, 105–115. [CrossRef]
29. Zang, M.; Zhao, C.; Wang, Y.; Chen, S. A review of recent advances in catalytic combustion of VOCs on perovskite-type catalysts. *J. Saudi Chem. Soc.* **2019**, *23*, 645–654. [CrossRef]
30. Topka, P.; Delaigle, R.; Kaluza, L.; Gaigneaux, E.M. Performance of platinum and gold catalysts supported on ceria-zirconia mixed oxide in the oxidation of chlorobenzene. *Catal. Today* **2015**, *253*, 172–177. [CrossRef]
31. López-Fonseca, R.; Gutiérrez-Ortiz, J.; Gonzalez-Velasco, J. Catalytic combustion of chlorinated hydrocarbons over H-BETA and PdO/H-BETA zeolite catalysts. *Appl. Catal. A Gen.* **2004**, *271*, 39–46. [CrossRef]
32. Giraudon, J.M.; Nguyen, T.B.; Leclercq, G.; Siffert, S.; Lamonier, J.F.; AboukaiS, A.; Vantomme, A.; Su, B.L. Chlorobenzene total oxidation over palladium supported on ZrO_2, TiO_2 nanostructured supports. *J. Catal.* **2008**, *137*, 379–384. [CrossRef]
33. Giraudon, J.M.; Elhachimi, A.; Leclercq, G. Catalytic oxidation of chlorobenzene over Pd/perovskites. *Appl. Catal. B Environ.* **2008**, *84*, 251–261. [CrossRef]
34. Dai, Q.; Bai, S.; Wang, Z.; Wang, X.; Lu, G. Catalytic combustion of chlorobenzene over Ru-doped ceria catalysts. *Appl. Catal. B Environ.* **2012**, *126*, 64–75. [CrossRef]
35. Dai, Q.; Bai, S.; Wang, J.; Li, M.; Wang, X.; Lu, G. The effect of TiO_2 doping on catalytic performances of Ru/CeO_2 catalysts during catalytic combustion of chlorobenzene. *Appl. Catal. B Environ.* **2013**, *142–143*, 222–233. [CrossRef]
36. Menéndez, B.M.; Fernández, E.D.; García, S.O.; Granda, A.V.; Sanz, F.D. Performance of different alumina-supported noble metal catalysts for the combustion of trichloroethylene at dry and wet conditions. *Appl. Catal. B Environ.* **2006**, *64*, 264–271.
37. Liu, X.; Chen, L.; Zhu, T.; Ning, R. Catalytic oxidation of chlorobenzene over noble metals (Pd, Pt, Ru, Rh) and the distributions of polychlorinated by-products. *J. Hazard. Mater.* **2019**, *363*, 90–98. [CrossRef]
38. Tian, M.; Guo, X.; Dong, R.; Guo, Z.; Shi, J.; Yu, Y.; Cheng, M.; Albilali, R.; He, C. Insight into the boosted catalytic performance and chlorine resistance of nanosphere-like meso-macroporous $CrO_x/MnCo_3O_x$ for 1,2-dichloroethane destruction. *Appl. Catal. B Environ.* **2019**, *259*, 118018. [CrossRef]
39. Tian, M.; Jian, Y.; Ma, M.; He, C.; Chen, C.; Liu, C.; Shi, J.-W. Rational design of $CrO_x/LaSrMnCoO_6$ composite catalysts with superior chlorine tolerance and stability for 1,2-dichloroethane deep destruction. *Appl. Catal. A Gen.* **2019**, *570*, 62–72. [CrossRef]
40. Tian, M.; He, C.; Yu, Y.; Pan, H.; Smith, L.; Jiang, Z.; Gao, N.; Jian, Y.; Hao, Z.; Zhu, Q. Catalytic oxidation of 1,2-dichloroethane over three-dimensional ordered meso-macroporous $Co_3O_4/La_{0.7}Sr_{0.3}Fe_{0.5}Co_{0.5}O_3$: Destruction route and mechanism. *Appl. Catal. A Gen.* **2018**, *553*, 1–14. [CrossRef]

41. Pasupulety, N.; Al-Zahrani, A.A.; Daous, M.A.; Driss, H.; Petrov, L.A. Methane aromatization study on M-Mo_2C/HZSM-5 (M = Ce or Pd or Nb) nano materials. *J. Mater. Res. Technol.* **2021**, *14*, 363–373. [CrossRef]
42. Zhang, K.; Dai, L.; Liu, Y.; Deng, J.; Jing, L.; Zhang, K.; Hou, Z.; Zhang, X.; Wang, J.; Feng, Y.; et al. Insights into the active sites of chlorine-resistant Pt-based bimetallic catalysts for benzene oxidation. *Appl. Catal. B Environ.* **2020**, *279*, 119372. [CrossRef]
43. Mohajeri, N.; Ali, T.; Bokerman, G.; Captain, J.E.; Peterson, B.V.; Whitten, M.; Trigwell, S.; Berger, C.; Brenner, J. TEM–XRD analysis of PdO particles on TiO_2 support for chemochromic detection of hydrogen. *Sensors Actuat. B Chem.* **2010**, *144*, 208–214. [CrossRef]
44. Mehdipour, M.; Tabaian, S.H.; Firoozi, S. Effect of IrO_2 crystallinity on electrocatalytic behavior of IrO_2–Ta_2O_5/MWCNT composite as anodes in chlor-alkali membrane cell. *Ceram. Int.* **2019**, *45*, 19971–19980. [CrossRef]
45. Ruan, M.; Song, P.; Liu, J.; Li, E.; Xu, W. Highly efficient regeneration of deactivated Au/C catalyst for 4-nitrophenol reduction. *J. Phys. Chem. C.* **2017**, *121*, 25882–25887. [CrossRef]
46. Lapham, D.P.; Lapham, J.L. BET surface area measurement of commercial magnesium stearate by krypton adsorption in preference to nitrogen adsorption. *Int. J. Pharmaceut.* **2019**, *568*, 118522. [CrossRef]
47. Wu, Q.; Yan, J.; Jiang, M.; Dai, Q.; Wu, J.; Ha, M.N.; Ke, Q.; Wang, X.; Zhan, W. Phosphate-assisted synthesis of ultrathin and thermally stable alumina nanosheets as robust Pd support for catalytic combustion of propane. *Appl. Catal. B Environ.* **2021**, *286*, 119949. [CrossRef]
48. Shi, Z.; Peng, Y.; Fei, T.; Zhou, R. New insight into the structure of CeO_2–TiO_2 mixed oxides and their excellent catalytic performances for 1,2-dichloroethane oxidation. *Chem. Eng. J.* **2016**, *295*, 99–108. [CrossRef]
49. Dai, Q.; Yin, L.-L.; Bai, S.; Wang, W.; Wang, X.; Gong, X.-Q.; Lu, G. Catalytic total oxidation of 1,2-dichloroethane over VO_x/CeO_2 catalysts: Further insights via isotopic tracer techniques. *Appl. Catal. B Environ.* **2016**, *182*, 598–610. [CrossRef]
50. Dai, Q.; Wang, W.; Wang, X.; Lu, G. Sandwich-structured CeO_2@ZSM-5 hybrid composites for catalytic oxidation of 1, 2-dichloroethane: An integrated solution to coking and chlorine poisoning deactivation. *Appl. Catal. B Environ.* **2017**, *203*, 31–42. [CrossRef]
51. Feng, X.; Tian, M.; He, C.; Li, L.; Shi, J.-W.; Yu, Y.; Cheng, J. Yolk-shell-like mesoporous $CoCrO_x$ with superior activity and chlorine resistance in dichloromethane destruction. *Appl. Catal. B Environ.* **2020**, *264*, 118493. [CrossRef]
52. Dai, Q.; Zhang, Z.; Yan, J.; Wu, J.; Johnson, G.; Sun, W.; Wang, X.; Zhang, S.; Zhan, W. Phosphate-functionalized CeO_2 nanosheets for efficient catalytic oxidation of dichloromethane. *Environ. Sci. Technol.* **2018**, *52*, 13430–13437. [CrossRef] [PubMed]
53. Chen, X.; Chen, X.; Yu, E.; Cai, S.; Jia, H.; Chen, J.; Liang, P. In situ pyrolysis of Ce-MOF to prepare CeO_2 catalyst with obviously improved catalytic performance for toluene combustion. *Chem. Eng. J.* **2018**, *344*, 469–479. [CrossRef]
54. Royer, S.; Duprez, D.; Can, F.; Courtois, X.; Batiot-Dupeyrat, C.; Laassiri, S.; Alamdari, H. Perovskites as substitutes of noble metals for heterogeneous catalysis: Dream or reality. *Chem. Rev.* **2015**, *45*, 10292–10368. [CrossRef] [PubMed]
55. Huang, H.; Gu, Y.; Zhao, J.; Wang, X. Catalytic combustion of chlorobenzene over VO_x/CeO_2 catalysts. *J. Catal.* **2015**, *326*, 54–68. [CrossRef]
56. Ji, K.; Dai, H.; Deng, J.; Song, L.; Gao, B.; Wang, Y.; Li, X. Three-dimensionally ordered macroporous $Eu_{0.6}Sr_{0.4}FeO_3$ supported cobalt oxides: Highly active nanocatalysts for the combustion of toluene. *Appl. Catal. B Environ.* **2013**, *129*, 539–548. [CrossRef]
57. Fang, L.; Yan, Z.; Wu, J.; Bugaev, A.; Lamberti, C.; Pera-Titus, M. Highly selective Ru/HBEA catalyst for the direct amination of fatty alcohols with ammonia. *Appl. Catal. B Environ.* **2021**, *286*, 119942. [CrossRef]
58. Larichev, Y.V.; Netskina, O.V.; Komova, O.V.; Simagina, V.I. Comparative XPS study of Rh/Al_2O_3 and Rh/TiO_2 as catalysts for $NaBH_4$ hydrolysis. *Int. J. Hydrogen Energ.* **2010**, *35*, 6501–6507. [CrossRef]
59. Feijen-Jeurissen, M.M.R.; Jorna, J.J.; Nieuwenhuys, B.E.; Sinquin, G.; Petit, C.; Hindermann, J.-P. Mechanism of catalytic destruction of 1,2-dichloroethane and trichloroethylene over γ-Al_2O_3 and γ-Al_2O_3 supported chromium and palladium catalysts. *Catal. Today* **1999**, *54*, 65–79. [CrossRef]
60. Chen, J.; Wu, Y.; Hu, W.; Qu, P.; Zhang, G.; Granger, P.; Zhong, L.; Chen, Y. New insights into the role of Pd-Ce interface for methane activation on monolithic supported Pd catalysts: A step forward the development of novel PGM Three-Way Catalysts for natural gas fueled engines. *Appl. Catal. B Environ.* **2020**, *264*, 118475. [CrossRef]
61. Yoon, D.; Kim, Y.; Lim, J.; Cho, B.; Hong, S.; Nam, I.-S.; Choung, J. Thermal stability of Pd-containing $LaAlO_3$ perovskite as a modern TWC. *J. Catal.* **2015**, *330*, 71–83. [CrossRef]
62. He, C.; Jiang, Z.; Ma, M.; Zhang, X.; Douthwaite, M.; Shi, J.-W.; Hao, Z. Understanding the Promotional Effect of Mn_2O_3 on Micro-/Mesoporous Hybrid Silica Nanocubic-Supported Pt Catalysts for the Low-Temperature Destruction of Methyl Ethyl Ketone: An Experimental and Theoretical Study. *ACS Catal.* **2018**, *8*, 4213–4229. [CrossRef]